Journal of Computational Physics 306 (2016) 117–136

Contents lists available at ScienceDirect

Journal of Computational Physics

www.elsevier.com/locate/jcp

Explicit filtering and exact reconstruction of the sub-filter stresses in large eddy simulation

Jonathan R. Bull [a,*], Antony Jameson [b]

[a] Division of Scientific Computing, Department of Information Technology, Uppsala University, Uppsala, Sweden
[b] Aerospace Computing Laboratory, Department of Aeronautics and Astronautics, Stanford University, Stanford, CA 94305, United States

ARTICLE INFO

Article history:
Received 23 September 2015
Received in revised form 3 November 2015
Accepted 19 November 2015
Available online 2 December 2015

Keywords:
Large eddy simulation
Differential filter
Defiltering
Deconvolution
Turbulent channel flow

ABSTRACT

Explicit filtering has the effect of reducing numerical or aliasing errors near the grid scale in large eddy simulation (LES). We use a differential filter, namely the inverse Helmholtz operator, which is readily applied to unstructured meshes. The filter is invertible, which allows the sub-filter scale (SFS) stresses to be exactly reconstructed in terms of the filtered solution. Unlike eddy viscosity models, the method of filtering and reconstruction avoids making any physical assumptions and is therefore valid in any flow regime. The sub-grid scale (SGS) stresses are not recoverable by reconstruction, but the second-order finite element method used here is an adequate source of numerical dissipation in lieu of an SGS model. Results for incompressible turbulent channel flow at $Re_\tau = 180$ are presented which show that explicit filtering and exact SFS reconstruction is a significant improvement over the standard LES approach of implicit filtering and eddy-viscosity SGS modelling.

© 2015 Elsevier Inc. All rights reserved.

1. Introduction

LES is a widely-used technique for high-fidelity numerical simulation of turbulent flows. By resolving large-scale flow features and modelling the effects of smaller scales, detailed studies of flows can be carried out without the extreme computational cost of direct numerical simulation (DNS). The separation of large and small scales is achieved by filtering the Navier–Stokes equations with a spatial filter operator, resulting in the appearance of a closure term representing the divergence of the unresolved stresses. This closure term is unknown and must be modelled somehow using information from the resolved scales. Considerable efforts have been expended on the 'closure problem' as surveyed by, for example, [1–3]. This paper is not concerned with model development or assessment, but with the reduction of numerical errors in solutions of the filtered Navier–Stokes equations.

Before proceeding we must distinguish between two types of filtering in LES. Firstly, the numerical discretisation and mesh truncate the unknown exact solution, acting like an implicit filter with a cutoff lengthscale (denoted $\triangle$) determined by the mesh resolution, resulting in a closure term representing scales below the grid scale: i.e., the sub-grid scale (SGS) stresses, denoted τ_{SGS}. Generally the exact form of the implicit filter operator is not known (although some have explored this topic [4–6]). Secondly, a filter operator with a cutoff lengthscale or 'width' $\widetilde{\triangle} > \triangle$ may be explicitly applied to the discrete equations. The filter is usually an integral operator with a specified kernel such as a Gaussian function. Then an additional closure term appears, representing grid-resolvable scales below the filter width $\widetilde{\triangle}$. These are called the sub-filter-scale (SFS) stresses, denoted τ_{SFS} (resolved SFS (RSFS) is sometimes used in the literature [7]).

* Corresponding author.
E-mail address: jonathan.bull@it.uu.se (J.R. Bull).

http://dx.doi.org/10.1016/j.jcp.2015.11.037
0021-9991/© 2015 Elsevier Inc. All rights reserved.

It may seem that additional modelling difficulties are introduced by explicit filtering, since both τ_{SFS} and τ_{SGS} have to be modelled. However, it is possible to exactly reconstruct τ_{SFS} in terms of the well-resolved wavenumbers by means of an invertible filter. Germano [8] proposed using a differential filter, namely the inverse Helmholtz operator, for which an exact inverse (defiltering) operator exists, enabling the SFS stresses to be exactly reconstructed. Exactly invertible filters were also investigated by Carati et al. [9], who proved that for any symmetric filter in one dimension, an exact expression could be derived as an infinite series expansion. They extended the idea to three dimensions by means of tensor products. Jameson also derived an exact expression for the SFS stresses in the compressible Navier–Stokes equations by using a generic invertible filter in the definition of the Favre-averaged variables [10]. Closely related methods are the approximate deconvolution (AD) [11] and velocity estimation techniques [12], whereby the filter is approximately inverted to generate a closure model for LES. These approaches have been successfully applied in a range of test cases [5,13,14].

A criticism leveled at exact reconstruction is that nothing is changed by explicitly filtering and adding back in exactly what was removed [5,9,15,16]. Certainly, this is true for the continuous system of PDEs. However, the discretised system has a distinct difference related to resolution of the turbulence spectrum. Typical numerical schemes exhibit increased dissipative and dispersive errors at the smaller scales close to $\triangle$. Explicit filtering is useful as a means of reducing the errors [17,18]. If the explicit filter width/cutoff frequency is chosen such that poorly resolved small scales/high frequencies (dependent on the numerical scheme [19]) are filtered out, then the remaining spectrum contains only well-resolved wavenumbers. The reconstructed SFS stress term only contains well-resolved wavenumbers [5,11]. Thus the procedure is akin to dealiasing and other filter-based stabilisation techniques. Furthermore, grid-converged LES solutions can be obtained by holding $\widetilde{\triangle}$ constant and refining $\triangle$, such that the modelling error is constant while the discretisation error is converged [20,21].

The inverse Helmholtz filter has been used by several researchers for LES [21–25]. Implementation of the filter in complex domains and on unstructured meshes is trivial because one simply needs to discretise and solve an elliptic equation using the existing numerical architecture. By contrast, integral filters, which essentially perform a weighted average over a patch of cells surrounding a node, are somewhat complicated to construct on unstructured meshes and in parallelised codes. Methods for constructing integral filters on unstructured meshes rely on complicated logic [26,27].

Exact reconstruction of the SFS stresses does not account for the SGS stresses, which are not directly recoverable from the resolved scales [9,28]. Additional modelling is required, for example with an eddy viscosity model [9,16]. We do not employ a model, but rely on numerical dissipation contributed by the second-order accurate stabilised finite element method used to discretise the equations. Approximation of the SGS stresses by numerical dissipation is broadly known as implicit LES (ILES). There is no guarantee that numerical dissipation represents the SGS dynamics [28], although it is an attractive approach for its simplicity and avoidance of the eddy-viscosity assumption.

In this paper, we apply explicit filtering and exact SFS reconstruction to LES of incompressible turbulent channel flow at $Re_\tau = 180$. Results show that the method leads to significantly improved predictions of bulk quantities (including skin friction) and first- and second-order flow quantities compared to the dynamic Smagorinsky model, no model, and explicit filtering only. The method does not rely on restrictive or inaccurate assumptions, such as the Boussinesq hypothesis or having the filter width sufficiently far down the inertial range, so it can be applied to any flow. It is formulated for arbitrary unstructured meshes and has the potential to improve the accuracy of LES of complex flows.

This paper is organised as follows. Section 2 introduces the filtering and reconstruction techniques. The exact reconstruction is derived and the commutation error is examined. Boundary conditions and similarities to other models are described. In Section 3, the stabilised finite element method is outlined and the numerical discretisation of the filter is presented. Section 4 presents the results of the turbulent channel flow validation case. Finally, Section 5 contains a discussion of the findings, conclusions and future work.

2. Explicit filtering and exact reconstruction of the SFS stresses

2.1. Filtered Navier–Stokes equations

We consider the incompressible Navier–Stokes equations for velocity $\mathbf{u} = \{u, v, w\}$ and pressure p in a domain $\Omega \in \mathcal{R}^3$ with a boundary Γ, at a sufficiently high Reynolds number Re that a turbulent energy cascade is present in the flow. Let us assume that the equations are discretised on a mesh that does not resolve the smallest scales of motion in the turbulent cascade, i.e. the computation is an LES rather than a DNS. The smallest scales are implicitly filtered out, and we denote the *implicitly filtered* solution by $\bar{\mathbf{u}}$. The implicitly filtered Navier–Stokes equations are

$$\begin{aligned} &\frac{\partial \bar{\mathbf{u}}}{\partial t} + \nabla \cdot (\overline{\mathbf{u}\mathbf{u}^T}) + \frac{1}{\rho}\nabla \bar{p} - \nu \nabla^2 \bar{\mathbf{u}} = 0, \\ &\nabla \cdot \bar{\mathbf{u}} = 0. \end{aligned} \tag{1}$$

The unknown closure term $\overline{\mathbf{u}\mathbf{u}^T}$ is replaced by

$$\overline{\mathbf{u}\mathbf{u}^T} = \bar{\mathbf{u}}\,\bar{\mathbf{u}}^T + \tau_{SGS}, \tag{2}$$

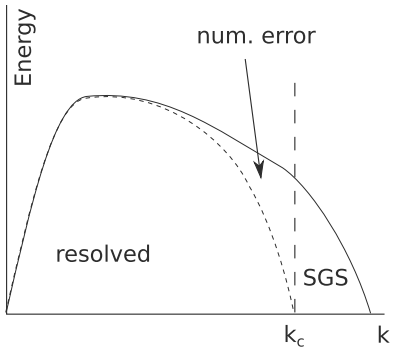

Fig. 1. Energy spectrum in LES with implicit filtering only.

where τ_{SGS} is the sub-grid scale (SGS) stress tensor. Therefore, in implicitly filtered LES we are solving

$$\frac{\partial \bar{\mathbf{u}}}{\partial t} + \nabla.(\bar{\mathbf{u}}\,\bar{\mathbf{u}}^T) + \frac{1}{\rho}\nabla \bar{p} - \nu\nabla^2\bar{\mathbf{u}} = \nabla \cdot \tau_{SGS}. \tag{3}$$

The energy spectrum in an LES is schematically represented in Fig. 1. All numerical schemes exhibit an increase in dissipative and dispersive errors near the grid cutoff wavenumber k_C (marked by a vertical dashed line). The presence of these errors causes the LES spectrum (fine dashed line) to fall off more sharply than the true spectrum (solid line) before the cutoff wavenumber. The region marked 'num. error' represents the missing energy that could theoretically be resolved on the grid by a 'perfect' scheme. The effect of the subgrid scales (the region marked SGS) on the resolved scales is usually approximated by a model, e.g. an eddy viscosity model to provide dissipation. If they a numerical source of dissipation is used in place of a model, such as a monotone upwind scheme, the term implicit LES (ILES) is often employed [29].

Now we consider the effect of applying an explicit filter to the discretised equations. Adopting the standard notation, an integral filter operator $\mathcal{G}$ is applied to $\bar{\mathbf{u}}$:

$$\widetilde{\bar{\mathbf{u}}} = \mathcal{G}[\bar{\mathbf{u}}] = \int_\Omega G(\mathbf{x}_0 - \mathbf{x})\bar{\mathbf{u}}(\mathbf{x}, t)d\mathbf{x}. \tag{4}$$

The filter kernel G is essentially a weighted average function over a local region characterised by a filter width, denoted $\widetilde{\Delta}$. Common examples are Gaussian and box (top-hat) functions. Applying the filter to the governing equations (1):

$$\begin{aligned} &\frac{\partial \widetilde{\bar{\mathbf{u}}}}{\partial t} + \nabla.(\widetilde{\bar{\mathbf{u}}\,\bar{\mathbf{u}}^T}) + \frac{1}{\rho}\nabla \widetilde{\bar{p}} - \nu\nabla^2\widetilde{\bar{\mathbf{u}}} = \nabla \cdot \widetilde{\tau_{SGS}}, \\ &\nabla \cdot \widetilde{\bar{\mathbf{u}}} = 0, \end{aligned} \tag{5}$$

where for simplicity it is assumed that filtering commutes with derivative operators. By making the substitution $\bar{\mathbf{u}} = \widetilde{\bar{\mathbf{u}}} + \bar{\mathbf{u}}'$, the closure term $\widetilde{\bar{\mathbf{u}}\,\bar{\mathbf{u}}^T}$ can be expanded as:

$$\widetilde{\bar{\mathbf{u}}\,\bar{\mathbf{u}}^T} = \widetilde{\widetilde{\bar{\mathbf{u}}}\,\widetilde{\bar{\mathbf{u}}}^T} + \widetilde{\widetilde{\bar{\mathbf{u}}}\,\bar{\mathbf{u}}'^T} + \widetilde{\bar{\mathbf{u}}'\,\widetilde{\bar{\mathbf{u}}}^T} + \widetilde{\bar{\mathbf{u}}'\,\bar{\mathbf{u}}'^T}. \tag{6}$$

We can define a sub-filter-scale (SFS) stress tensor by the *double decomposition*:

$$\begin{aligned} \tau_{SFS} &= \widetilde{\bar{\mathbf{u}}\bar{\mathbf{u}}^T} - \widetilde{\widetilde{\bar{\mathbf{u}}}\,\widetilde{\bar{\mathbf{u}}}^T} \\ &= \widetilde{\widetilde{\bar{\mathbf{u}}}\,\bar{\mathbf{u}}'^T} + \widetilde{\bar{\mathbf{u}}'\,\widetilde{\bar{\mathbf{u}}}^T} + \widetilde{\bar{\mathbf{u}}'\,\bar{\mathbf{u}}'^T}. \end{aligned} \tag{7}$$

The first two terms are the cross terms and the last is the SGS Reynolds stress term. With this definition, the filtered momentum equation is

$$\frac{\partial \widetilde{\bar{\mathbf{u}}}}{\partial t} + \nabla.(\widetilde{\widetilde{\bar{\mathbf{u}}}\,\widetilde{\bar{\mathbf{u}}}^T}) + \frac{1}{\rho}\nabla \widetilde{\bar{p}} - \nu\nabla^2\widetilde{\bar{\mathbf{u}}} = \nabla \cdot \widetilde{\tau_{SGS}} + \nabla \cdot \tau_{SFS}. \tag{8}$$

This form has the advantage that the advection term does not contain frequencies above the cutoff of the filter. However, it precludes the use of splitting schemes for the advection term. It also prevents the use of energy-stable skew-symmetric schemes, as noted by various authors [20,30], due to the fact that

$$\int_\Omega \widetilde{\bar{u}}_i \frac{\partial \widetilde{\bar{u}}_i\,\widetilde{\bar{u}}_j}{\partial x_j} d\Omega \neq 0. \tag{9}$$

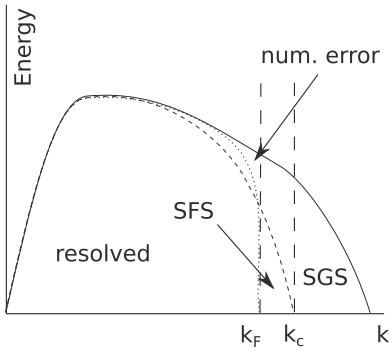

Fig. 2. Energy spectrum in LES with implicit and explicit filtering and SFS stress reconstruction.

When using the differential filter (see below), energy stability can be proven for constant filter width [31] and (in a non-standard Sobolev norm) spatially varying filter with a restriction on the second derivative of $\widetilde{\triangle}$ [30].

To avoid these difficulties, we employ the Leonard decomposition:

$$\tau_{SFS} = \widetilde{\bar{\mathbf{u}}\,\bar{\mathbf{u}}^T} - \widetilde{\bar{\mathbf{u}}}\,\widetilde{\bar{\mathbf{u}}}^T. \tag{10}$$

Now the filtered momentum equation reads

$$\frac{\partial \widetilde{\bar{\mathbf{u}}}}{\partial t} + \nabla.(\widetilde{\bar{\mathbf{u}}}\,\widetilde{\bar{\mathbf{u}}}^T) + \frac{1}{\rho}\nabla\widetilde{\bar{p}} - \nu\nabla^2\widetilde{\bar{\mathbf{u}}} = \nabla\cdot\widetilde{\tau_{SGS}} + \nabla\cdot\tau_{SFS}, \tag{11}$$

and the advection term can be discretised with a split or skew-symmetric scheme. Although the explicitly filtered velocity contains only frequencies up to k_F, the advection term can have higher frequencies. However, if the filter cutoff frequency satisfies $k_F \leq k_C/2$ (equivalently $\widetilde{\triangle} \geq 2\triangle$) then the whole spectrum of the advection term is resolvable on the mesh.

Unlike the SGS stresses, the resolved SFS stresses – those lying between the grid and filter cutoff frequencies k_C and k_F – are recoverable from $\bar{\mathbf{u}}$, either by exact or AD procedures. The advantage of doing so is that this crucial portion of the turbulent energy spectrum is transferred to lower wavenumbers which are less affected by numerical errors. Fig. 2 shows an improved spectrum (dotted line) obtained by explicit filtering and reconstruction of the SFS stresses (so-called soft deconvolution [1]). Note that the energy in the resolved wavenumbers close to k_F is closer to the true turbulent spectrum.

There is a growing literature on the benefits of explicit filtering on error control in LES [7,17,18,21,32–34], although crossover into practical applications has been limited thus far. By refining the mesh resolution and holding $\widetilde{\triangle}$ (resp. k_F) constant, it is possible to demonstrate grid convergence of LES solutions. In theory, the greater the ratio $\gamma = k_C/k_F$ ($\gamma = \widetilde{\triangle}/\triangle$ in the physical domain), the smaller the effect of numerical errors on the resolved scales. Nevertheless, by setting γ large, one reduces the richness of information in the 'usable' solution. Guidance on the optimal ratio between k_C and k_F can be found by looking at the departure of the numerical wavenumber from the true wavenumber for the numerical scheme under consideration. One can also observe the effect on the accuracy of LES results, as is done in this paper.

Aside from these considerations, the grid cutoff is still required to be sufficiently far down in the inertial range that the SGS stresses can be well-approximated by a subgrid model or numerical dissipation. However, it is worth noting that the SGS stresses contain wavenumbers no lower than k_C. Thus, if the explicit filter transfer function is close to zero at k_C:

$$\widetilde{\tau_{SGS}} = \widetilde{\overline{\mathbf{u}\mathbf{u}^T}} - \widetilde{\bar{\mathbf{u}}\,\bar{\mathbf{u}}^T} \approx 0. \tag{12}$$

2.2. Invertible filter

For simplicity of notation, we now drop the double-filtered notation $\widetilde{\bar{\mathbf{u}}}$ and denote the implicitly and explicitly filtered solutions by $\mathbf{u}$ and $\widetilde{\mathbf{u}} = \mathcal{G}[\mathbf{u}]$ respectively. The filter operator (4) was of integral type. However, in this paper we consider a differential filter, namely the inverse Helmholtz differential operator:

$$\widetilde{\mathbf{u}} = \mathcal{G}[\mathbf{u}] = (1 - \alpha^2\nabla^2)^{-1}\mathbf{u}. \tag{13}$$

The filter can equivalently be expressed as an integral (convolution) operator with the kernel

$$G(\mathbf{x} - \mathbf{x}') = \frac{1}{4\pi\widetilde{\triangle}^2}\frac{\exp(-|\mathbf{x} - \mathbf{x}'|/\widetilde{\triangle})}{|\mathbf{x} - \mathbf{x}'|}. \tag{14}$$

Fig. 3 shows the filter kernel function for $r = |\mathbf{x} - \mathbf{x}'| \in [-1.5, 1.5]$ (note the singularity at $r = 0$ is differentiable). The smoothing parameter α is related to the filter width $\widetilde{\triangle}$. Note that α can be chosen freely and any positive value of α has a smoothing effect. For example, a value of $\alpha^2 = \widetilde{\triangle}^2/40$ can be derived by equating the second moment of the filter kernel

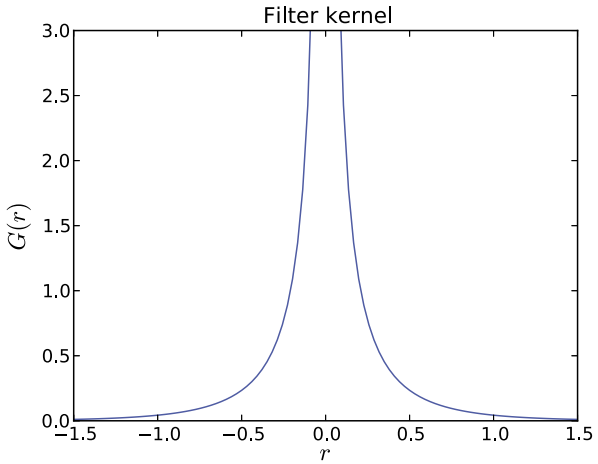

Fig. 3. Kernel function of the inverse Helmholtz filter.

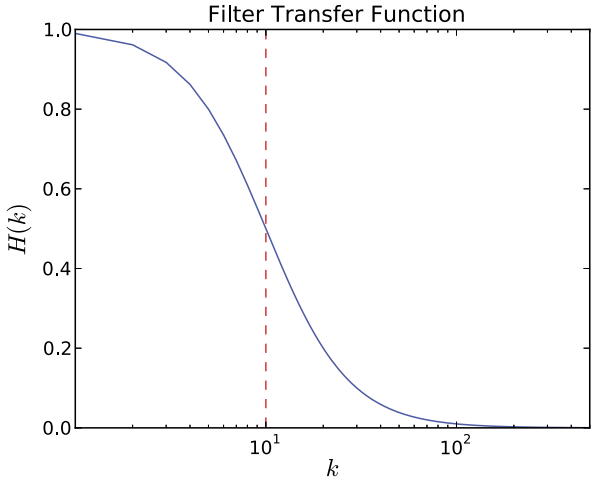

Fig. 4. Transfer function of the inverse Helmholtz filter.

to the second moment of the spherical top-hat kernel [26]. In this paper we use the definition $\alpha^2 = \widetilde{\triangle}^2/24$ so that (13) approximates the Gaussian filter of width $\widetilde{\triangle}$. The filter width is defined as a positive constant multiplied by the element size: $\widetilde{\triangle} = C\triangle$. As a consequence of the freedom of choice of α, C can be less than one. This stands in contrast to integral filters, where $C \geq 2$ because of the Nyquist theorem. We use Deardorff's [35] general definition of element size in three dimensions: $\triangle = \sqrt[3]{\text{Vol.}}$

The Fourier transform of the differential filter (13) is defined by

$$\widetilde{\hat{\mathbf{u}}}(k) = \hat{G}(k)\hat{\mathbf{u}}(k) = \frac{1}{1+\alpha^2 k^2}\hat{\mathbf{u}}(k), \tag{15}$$

which is plotted in Fig. 4 for positive k. Also shown (vertical dashed line) is the cutoff frequency k_F, defined as the wavenumber satisfying $\hat{G}(k_F) = 0.5$. Clearly the filter has a broadband effect but is stronger at higher wavenumbers.

The existence of an inverse (defiltering) operator is evident from (13):

$$\mathcal{Q} = \mathcal{G}^{-1} = \left(1 - \alpha^2\nabla^2\right). \tag{16}$$

It was noted by Germano [36] that (13) and (16) could be used to derive an exact expression for the resolved SFS stress tensor (10). The derivation begins by expressing velocity products in terms of filtered velocities:

$$\mathbf{u}\mathbf{u}^T = (\widetilde{\mathbf{u}} - \alpha^2\nabla^2\widetilde{\mathbf{u}})(\widetilde{\mathbf{u}} - \alpha^2\nabla^2\widetilde{\mathbf{u}})^T, \tag{17}$$

$$\widetilde{\mathbf{u}}\,\widetilde{\mathbf{u}}^T = \mathcal{G}[\widetilde{\mathbf{u}}\,\widetilde{\mathbf{u}}^T] - \alpha^2\nabla^2(\mathcal{G}[\widetilde{\mathbf{u}}\,\widetilde{\mathbf{u}}^T]). \tag{18}$$

Applying the filter to (17):

$$\begin{aligned}\mathcal{G}[\mathbf{u}\mathbf{u}^T] &= \mathcal{G}[(\widetilde{\mathbf{u}} - \alpha^2\nabla^2\widetilde{\mathbf{u}})(\widetilde{\mathbf{u}} - \alpha^2\nabla^2\widetilde{\mathbf{u}})^T] \\ &= \mathcal{G}[\widetilde{\mathbf{u}}\,\widetilde{\mathbf{u}}^T - \alpha^2(\widetilde{\mathbf{u}}\,\nabla^2\widetilde{\mathbf{u}}^T + \widetilde{\mathbf{u}}^T\,\nabla^2\widetilde{\mathbf{u}}) + \alpha^4\nabla^2\widetilde{\mathbf{u}}\,\nabla^2\widetilde{\mathbf{u}}^T]. \end{aligned} \tag{19}$$

Now the SFS stress tensor is

$$\tau_{SFS} = \mathcal{G}[-\alpha^2(\widetilde{\mathbf{u}}\,\nabla^2\widetilde{\mathbf{u}}^T + \widetilde{\mathbf{u}}^T\,\nabla^2\widetilde{\mathbf{u}}) + \alpha^4\nabla^2\widetilde{\mathbf{u}}\,\nabla^2\widetilde{\mathbf{u}}^T] + \alpha^2\nabla^2(\mathcal{G}[\widetilde{\mathbf{u}}\,\widetilde{\mathbf{u}}^T]). \tag{20}$$

If we assume that α is constant and that filtering commutes with differentiation (these are in fact the same criterion), then the last term in (20) can be rewritten:

$$\tau_{SFS} = \mathcal{G}[-\alpha^2(\widetilde{\mathbf{u}}\,\nabla^2\widetilde{\mathbf{u}}^T + \widetilde{\mathbf{u}}^T\,\nabla^2\widetilde{\mathbf{u}}) + \alpha^4\nabla^2\widetilde{\mathbf{u}}\,\nabla^2\widetilde{\mathbf{u}}^T + \alpha^2\nabla^2(\widetilde{\mathbf{u}}\,\widetilde{\mathbf{u}}^T)]. \tag{21}$$

The product rule of differentiation leads to the following identity:

$$\nabla(a(x)b(x)) = a\nabla b + b\nabla a \quad \therefore \nabla^2(a(x)b(x)) = 2\nabla a\nabla b + a\nabla^2 b + b\nabla^2 a. \tag{22}$$

Using this identity allows (21) to be simplified:

$$\tau_{SFS} = \mathcal{G}[2\alpha^2\nabla\widetilde{\mathbf{u}}\,\nabla\widetilde{\mathbf{u}}^T + \alpha^4\nabla^2\widetilde{\mathbf{u}}\nabla^2\widetilde{\mathbf{u}}^T]. \tag{23}$$

Therefore, the exact SFS stress is obtained by solving the elliptic equation

$$\mathcal{Q}\tau_{SFS} = (1 - \alpha^2\nabla^2)\tau_{SFS} = 2\alpha^2\nabla\widetilde{\mathbf{u}}\,\nabla\widetilde{\mathbf{u}}^T + \alpha^4\nabla^2\widetilde{\mathbf{u}}\,\nabla^2\widetilde{\mathbf{u}}^T, \tag{24}$$

which is in fact six scalar equations for the six independent components of τ_{SFS}. Equation (24) requires boundary conditions to be specified; this is dealt with in Section 2.5. Note that, by inspection, τ_{SFS} is non-negative. Therefore, no backscattering of energy from the SFS to the resolved scales is permitted: the method acts only to drain energy from the resolved scales.

Although (24) is somewhat expensive to solve, so are some AD models, which use repeated filtering to obtain approximations to the inverse operation via the van Cittert procedure. For example, Stolz et al. [11] proposed using five levels of filtering; for three velocity components that requires 15 applications of the filter. The issue is compounded if the compressible Navier–Stokes equations are being solved, with five variables to contend with.

2.3. Commutation error

In the derivation of (24), it was assumed that α was constant. In general, the computational mesh will have spatially varying resolution, so it is desirable to allow the filter width to vary, rather than specifying a single filter width across the entire mesh. However, a *commutation error* is introduced because filtering does not commute with derivative operators when the filter width varies. For example,

$$\nabla(\mathcal{G}[\mathbf{u}]) \neq \mathcal{G}[\nabla\mathbf{u}], \tag{25}$$

and the difference is the commutation error between the filter and gradient operators.

Adding $\mathcal{G}[\alpha^2\nabla^2(\widetilde{\mathbf{u}}\,\widetilde{\mathbf{u}}^T)]$ to the first term in (20) and applying the identity (22), then subtracting $\mathcal{G}[\alpha^2\nabla^2(\widetilde{\mathbf{u}}\,\widetilde{\mathbf{u}}^T)]$ from the final term in (20), leads to an expression for the SFS stresses without assuming $\alpha =$ constant:

$$\begin{aligned}\tau_{SFS} &= \mathcal{G}[2\alpha^2\nabla\widetilde{\mathbf{u}}\,\nabla\widetilde{\mathbf{u}}^T + \alpha^4\nabla^2\widetilde{\mathbf{u}}\,\nabla^2\widetilde{\mathbf{u}}^T] + \epsilon, \\ \epsilon &= \alpha^2\nabla^2(\mathcal{G}[\widetilde{\mathbf{u}}\,\widetilde{\mathbf{u}}^T]) - \mathcal{G}[\alpha^2\nabla^2(\widetilde{\mathbf{u}}\,\widetilde{\mathbf{u}}^T)]. \end{aligned} \tag{26}$$

The term ϵ is recognised as the commutation error between filtering and the operator $\alpha^2\nabla^2$. The error is $\mathcal{O}(\widetilde{\triangle}^2)$, and could thus be neglected when using a second-order accurate numerical method, except for the fact that the second term is also $\mathcal{O}(\nabla^2(\alpha^2))$. If the mesh size is varied linearly in the domain interior, i.e. $\widetilde{\triangle} = \mathcal{O}(\mathbf{x})$ away from boundaries, then $\nabla^2(\alpha^2) = \mathcal{O}(1)$ and $\epsilon = \mathcal{O}(\alpha^2)$. At the boundary the mesh size is discontinuous and a boundary commutation error is committed. This order-of-magnitude analysis of the commutation error suggests that by carefully constructing the mesh so that element size varies smoothly and no faster than linearly, then the interior error might be safely ignored. Alternatively, the full expression for the SFS stresses including commutation error terms (26) could be included in the flow solver. However, the computational expense of additional filter operations is unattractive.

2.4. Similarities to other models

The second-order term in (24) is similar to the gradient model [37]:

$$\tau_{SFS} = 2\alpha^2\nabla\widetilde{\mathbf{u}}\,\nabla\widetilde{\mathbf{u}}^T. \tag{27}$$

The gradient model has the tendency to amplify high wavenumbers and increase the kinetic energy of solutions of the filtered Navier–Stokes equations [38]. Upon applying the inverse Helmholtz filter to the gradient model one obtains the rational LES (RLES) model [38]:

$$\tau_{SFS} = (1 - \alpha^2\nabla^2)^{-1}\left(2\alpha^2\nabla\widetilde{\mathbf{u}}\,\nabla\widetilde{\mathbf{u}}^T\right). \tag{28}$$

This model was found to damp high-frequency oscillations and make good predictions of turbulent channel flow [39]. The only difference between the exact SFS and RLES models is a fourth-order term; the influence of this term on simulations of turbulent channel flow is assessed in Section 4.

2.5. Boundary conditions

There are several possibilities to consider when setting boundary conditions on the inverse Helmholtz-filtered velocity and SFS stresses. The simplest option is based on the argument that the filter width should vanish at the wall, making (13) singular and enforcing $\widetilde{\mathbf{u}} = \mathbf{u}$ at the wall. This amounts to a no-slip condition on $\bar{\mathbf{u}}$ for wall-bounded flows. By the same argument and for consistency, the exact SFS reconstruction must satisfy $\tau_{SFS} = 0$ at the wall. Thus, homogeneous Dirichlet boundary conditions are imposed on (24).

However, an argument going back to Navier in 1827 states that a moving fluid should satisfy zero-penetration and slip-with-friction boundary conditions [38]. Serrin [40] presented experimental justification for this in high Reynolds number gaseous flows. Layton [41] suggested that the no-slip condition on a discrete velocity field could also be relaxed, either by a Lagrange multiplier formulation, a penalty term or a slip-with-friction condition. Galdi and Layton [38] proposed the following zero-penetration, slip-with-friction (Robin) boundary conditions for the filtered velocity:

$$\widetilde{\mathbf{u}} \cdot \mathbf{n} = 0, \tag{29}$$

$$\mathbf{u} \cdot \mathbf{t} = \widetilde{\mathbf{u}} \cdot \mathbf{t} - \beta\frac{\partial}{\partial n}(\widetilde{\mathbf{u}} \cdot \mathbf{t}) = 0, \tag{30}$$

where $\mathbf{n}$ is the normal to the wall, $\mathbf{t} = (t_1, t_2)$ is the system of orthogonal tangents to the surface and β is a slip (friction) coefficient to be determined. Bose and Moin [42] showed that a limited-slip condition can be derived by considering a variant of the inverse Helmholtz filter:

$$\widetilde{\mathbf{u}} - \frac{\partial}{\partial x_k}\left(l_p\frac{\partial\widetilde{\mathbf{u}}}{\partial x_k}\right) = \mathbf{u}, \tag{31}$$

where l_p is related to the filter width variation. Expanding (31) and evaluating at the wall gives

$$\widetilde{\mathbf{u}} - \frac{\partial l_p}{\partial x_k}\frac{\partial\widetilde{\mathbf{u}}}{\partial x_k} = 0. \tag{32}$$

Assuming that l_p does not vary in directions parallel to the wall, this simplifies to

$$\widetilde{\mathbf{u}} - \frac{\partial l_p}{\partial n}\frac{\partial\widetilde{\mathbf{u}}}{\partial n} = 0. \tag{33}$$

For dimensional consistency, $\frac{\partial l_p}{\partial n}$ must represent a lengthscale and can be related to the filter width. By comparison with (29), it also represents a friction coefficient:

$$\beta = \frac{\partial l_p}{\partial n}. \tag{34}$$

It can be argued that as the filter width becomes very small (as in a wall-resolved LES or DNS), (33) converges to the no-slip condition. In the context of wall-modelled LES, we are free to specify β. However, it is not obvious how to do so without introducing new assumptions or tunable parameters. The approach taken by Bose and Moin [42] was to use a dynamic procedure taking information from the local flow, akin to Germano's dynamic method for the Smagorinsky coefficient. They were able to accurately predict the separation point on an airfoil at stall conditions using this method.

An exact SFS stress reconstruction can be derived from the filter variant (31), although it is complicated by the presence of first and second derivatives of l_p. If condition (33) is imposed on $\widetilde{\mathbf{u}}$, then τ_{SFS} can be equipped with consistent boundary conditions, derived using (33):

$$\tau_{SFS}|_{y=0} = \widetilde{\mathbf{u}}\widetilde{\mathbf{u}}^T - \widetilde{\mathbf{u}\mathbf{u}^T} = \beta^2\left(\frac{\partial\widetilde{\mathbf{u}}}{\partial n}\right)\left(\frac{\partial\widetilde{\mathbf{u}}}{\partial n}\right)^T. \tag{35}$$

The investigation of limited-slip boundary conditions on $\widetilde{\mathbf{u}}$ is left as the subject of future research. In this paper, we employ no-slip boundary conditions and perform wall-resolved LES.

3. Numerical discretisation and implementation

3.1. Stabilised finite element method

The methods developed are implemented in the open-source finite element CFD code Fluidity [43,44]. A continuous Galerkin finite element method is used with piecewise linear basis functions for the velocity and pressure ($P1$ CG–$P1$

CG). This element pair is LBB-unstable and can introduce spurious pressure modes on collocated grids. Using a higher-dimensional space for velocity, such as the $P2$ CG–$P1$ CG discretisation, does satisfy the LBB criterion [45]. However, it has been found that $P1$ CG–$P1$ CG is the better choice for LES owing to its superior treatment of the velocity–pressure gradient correlation, which drives energy exchanges between velocity components [46]. These exchanges are important because they affect the small-scale flow dynamics, while spurious pressure modes are negligible on unstructured meshes [46]. Stabilisation of the $P1$ CG–$P1$ CG element pair is achieved by including a fourth-order pressure derivative term into the continuity equation [47,48]. The disadvantage is that the continuity equation is no longer exactly satisfied, i.e. the velocity field is not divergence-free.

3.2. Discretised inverse Helmholtz filter

Using the continuous Galerkin finite element method, the inverse Helmholtz filter (13) applied to a field $\mathbf{u}^h \in \mathcal{U}^h$, weighted with a test function $\mathbf{w}^h \in \mathcal{W}^h$ and integrated over a bounded domain Ω can be written:

Given $\mathbf{u}^h \in \mathcal{U}^h$, find a filtered field $\widetilde{\mathbf{u}}^h \in \mathcal{U}^h$ such that

$$\int_\Omega \widetilde{\mathbf{u}}^h \mathbf{w}^h d\Omega - \int_\Omega \nabla \cdot \frac{\widetilde{\triangle}^2}{24} \nabla \widetilde{\mathbf{u}}^h \mathbf{w}^h d\Omega = \int_\Omega \mathbf{u}^h \mathbf{w}^h d\Omega, \quad \forall \mathbf{w}^h \in \mathcal{W}^h. \tag{36}$$

Using Green's first identity on the Laplacian ($\nabla \cdot \nabla$) term, (36) is written

$$\int_\Omega \widetilde{\mathbf{u}}^h \mathbf{w}^h d\Omega + \int_\Omega \nabla \mathbf{w}^h \cdot \frac{\widetilde{\triangle}^2}{24} \nabla \widetilde{\mathbf{u}}^h d\Omega - \int_\Gamma \mathbf{w}^h \frac{\widetilde{\triangle}^2}{24} \nabla \widetilde{\mathbf{u}}^h \cdot \mathbf{n}\, d\Gamma = \int_\Omega \mathbf{u}^h \mathbf{w}^h d\Omega, \tag{37}$$

where $\mathbf{n}$ is the surface normal. An integral over the domain boundary Γ has appeared allowing the imposition of a weak Neumann boundary condition; neglecting the term implicitly imposes a homogeneous Neumann condition. Choosing identical test and trial spaces $\mathcal{U}^h$ and $\mathcal{W}^h$ and linear shape functions N_i we write the matrix equation over an element Ω^e:

$$\widetilde{\mathbf{u}}^e = \left[G^e_{\text{Helm}}\right]^{-1} \mathbf{u}^e,$$
$$\left[G^e_{\text{Helm}}\right]_{ij} = \int_{\Omega^e} N_i N_j d\Omega + \int_{\Omega^e} \nabla N_i \cdot \frac{\widetilde{\triangle}^2}{24} \nabla N_j d\Omega. \tag{38}$$

4. Turbulent channel flow at $Re_\tau = 180$

We use the 3D periodic channel flow at $Re_\tau = 180$, for which DNS data is available from Kim et al. [49], to validate the exact SFS reconstruction. The domain has dimensions $L_x = 2\pi$, $L_y = 1$, $L_z = \pi$ and the coordinates are chosen such that $0 \leq x \leq 2\pi$, $-0.5 \leq y \leq 0.5$, $0 \leq z \leq \pi$.

4.1. Simulation setup

Besides the exact SFS reconstruction, the following simulations were performed:

- implicit filtering, no SGS model
- explicit filtering, no SFS model
- implicit filtering, dynamic Smagorinsky SGS model
- explicit filtering, dynamic Smagorinsky SFS model
- explicit filtering, rational LES SFS model

We refer to the model as 'SGS' if no explicit filtering is performed, otherwise as 'SFS'. The dynamic Smagorinsky model employed inverse Helmholtz test filtering [25]. Whether implicitly or explicitly filtering, the model is a function of the filter width $\widetilde{\triangle}$; the value of filter width:mesh size ratio $\gamma = 1$ was chosen for the current tests. With the exact SFS reconstruction, sensitivity to γ was assessed across the range $\gamma = \{0.5, 1, 2, 4\}$.

Three structured hexahedral meshes were generated, and the cells split into tetrahedra, using the free meshing package Gmsh [50]. Wall-normal resolution was specified so that the boundary layers were well resolved and increased with a linear stretching function towards the channel centre. Uniform resolution was prescribed in the streamwise (x) and spanwise (z) directions. The meshes are summarised in Table 1. Also listed are the computed C_f and Re_τ using explicit filtering and exact SFS with $\gamma = 1$, showing convergence towards the DNS values. Unless otherwise stated, all simulations presented hereafter used the fine mesh.

Table 1
Mesh resolution in turbulent channel flow. Quantities in wall units are based on friction velocities using explicit filtering and exact SFS ($\gamma = 1$) on each mesh.

Mesh	N_x	N_y	N_z	NDOF	Δx^+	Δy^+	Δz^+	Re_τ	$C_f \times 10^3$
DNS	**192**	**129**	**160**	**3.96M**	**12**	**0.05**	**7**	**180**	**8.18**
crs	36	32	36	41,472	59.4	1.7	29.7	170.3	7.15
med	48	44	48	101,376	43.1	1.2	21.5	164.6	7.48
fine	96	64	48	294,912	24.1	0.9	24.1	184.5	7.68

Table 2
Computed flow parameters from LES simulations versus DNS. Effect of γ in exact SFS model.

Model	Re_δ	Re_τ	U_B/U_τ	U_C/U_B	$C_f \times 10^3$
DNS	**3440**	**180**	**15.63**	**1.16**	**8.18**
exact SFS ($\gamma = 0.5$)	4143.4	212.6	17.09	1.141	6.85
exact SFS ($\gamma = 1$)	2975.7	184.5	16.14	1.157	7.68
exact SFS ($\gamma = 2$)	2206.3	150.0	14.70	1.189	9.25
exact SFS ($\gamma = 4$)	1524.5	119.3	12.78	1.237	12.25

All simulations used the stabilised $P1$ CG–$P1$ CG formulation described above. The time derivative was approximated by a central difference and the timestep was limited by $CFL \leq 2$, giving typical timesteps of about 0.05–0.08 seconds. Time marching was by the Picard iteration method with two nonlinear iterations per timestep and a nonlinear relaxation coefficient of 0.5. Solution of the discretised pressure and velocity equations employed the CG and GMRES solvers respectively, and SOR preconditioning, in the PETSc library [51]. CG/SOR was also used to solve (13) for the filtered velocity and (24) for the exact SFS stress. A relative error tolerance of 1.0×10^{-7} was set for all solves.

A fourth-order polynomial initial condition was specified:

$$u(y) = 1.875 - 15y^2 + 30y^4, \tag{39}$$

resulting in a bulk velocity $u_B = 1.0$. The molecular viscosity was set at $\nu = 1.453 \times 10^{-4}$ corresponding to a bulk Reynolds number of $Re_\delta = 3440$ based on channel half-width $\delta = 0.5$. Using the method of Andersson et al. [52], an initial perturbation in the vertical direction was prescribed to initiate the turbulent cascade:

$$v(x, y, z) = 0.1 \exp\left[-\left(\frac{x - L_x/2}{L_x}\right)^2\right] \exp\left[-\left(\frac{y}{L_y}\right)^2 \cos 4(z - L_z/2)\right]. \tag{40}$$

Statistics were computed during the simulation, starting after 200 seconds of flow time (≈30 convection periods), which was found to be sufficient for the L_2 norm of the velocity field to reach quasi-steady state, i.e. for the initial transient to decay. Sampling took place every timestep for at least 400 seconds (60 convection periods). Time-averaged quantities are denoted by angle brackets, e.g. $\langle \mathbf{u} \rangle$. To force the flow to a steady state, a constant streamwise pressure gradient was prescribed. The Blasius correlation for fully developed turbulent flow gave an estimated friction factor of $f \approx 0.042$, equating to a pressure gradient of $dP/dx = 8.67 \times 10^{-3}$. The actual bulk velocities obtained at steady state deviated slightly from 1.0 because the imposed pressure gradient tended to be too high during the initial flow development. However, the deviation is not considered large enough to have a significant effect on the results.

To estimate the wall shear stress, the wall-normal gradient of the time-averaged streamwise velocity $\partial \langle u \rangle / \partial y$ was calculated by a linear approximation within the wall-adjacent element. In addition to time averaging, the velocity and Reynolds stresses were averaged over homogeneous directions in postprocessing with a grid of 40 × 40 evenly-spaced sampling locations. Unless stated otherwise, all quantities were averaged in time and space.

4.2. Bulk quantities

Tables 2 and 3 show the computed bulk and friction Reynolds numbers Re_δ and Re_τ, ratio of bulk to friction velocity U_B/U_τ, ratio of mean centerline to bulk velocity U_C/U_B, and skin friction coefficient C_f for the current simulations versus the DNS data. In Table 2, the filter width to mesh size ratio γ is varied in the exact SFS model. Higher values give lower Reynolds numbers, indicating an increase in dissipation. The best agreement of all parameters with the DNS data is at $\gamma = 1$. U_B/U_τ, U_C/U_B and C_f are in very good agreement, suggesting that the free-stream and near-wall mean profiles are well captured. The Reynolds numbers suggest that the exact SFS model provides the correct amount of energy drainage to counterbalance the imposed pressure gradient.

In Table 3, different models are compared with $\gamma = 1$. Explicit filtering (no model) has very little effect compared to the unfiltered case (no model). The dynamic LES results are inaccurate and do not differ much from the no-model results; filtering makes very little difference here either. The rational LES and exact SFS results are far more accurate. Furthermore, they are almost identical, suggesting that the fourth-order term in the exact SFS reconstruction is insignificant in this test.

Table 3
Computed flow parameters from LES simulations versus DNS. Comparison of models with $\gamma = 1$.

Model	Re_δ	Re_τ	U_B/U_τ	U_C/U_B	$C_f \times 10^3$
DNS	**3440**	**180**	**15.63**	**1.16**	**8.18**
no model, unfiltered	4126.7	232.1	17.78	1.132	6.33
no model, filtered	4144.6	234.1	17.70	1.129	6.38
dynamic, unfiltered	4329.3	216.8	19.97	1.126	5.02
dynamic, filtered	4315.6	216.2	19.96	1.123	5.02
rational LES	2987.0	184.1	16.22	1.155	7.59
exact SFS	2975.7	184.5	16.12	1.157	7.68

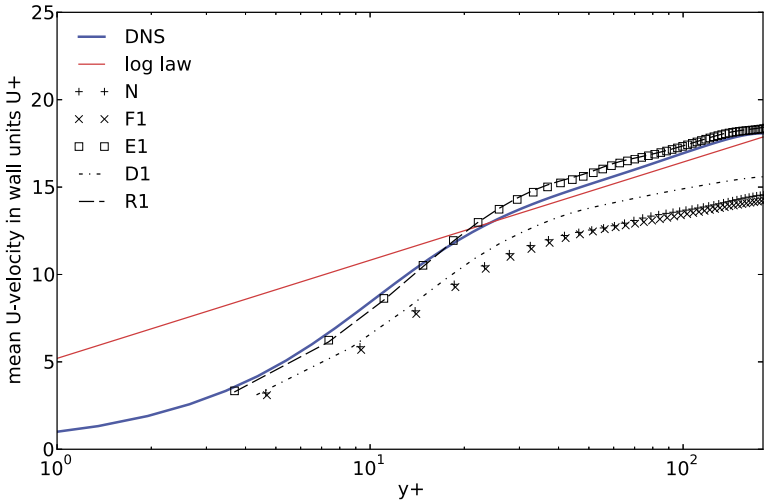

(a) Model comparison

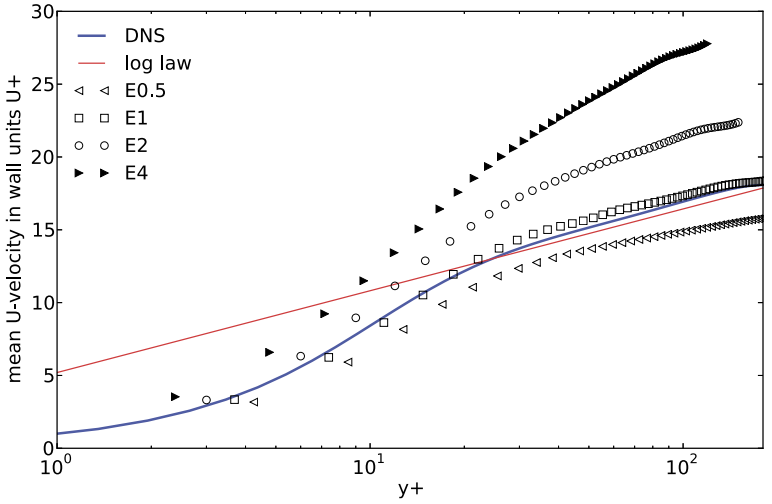

(b) Effect of γ

Fig. 5. Time- and space-averaged velocity in wall units $\langle u^+ \rangle$. N = implicit filter/no model, F1 = explicit filter/no model ($\gamma = 1$), E0.5/1/2/4 = exact SFS ($\gamma = 0.5/1/2/4$), D = implicit filter/dynamic model ($\gamma = 1$), R = explicit filter/Rational LES model ($\gamma = 1$).

4.3. Mean velocity

Fig. 5 shows the time- and space-averaged velocity $\langle u^+ \rangle$ in wall units for the current simulations versus the DNS data. Also shown is the empirical log law of the wall, $\langle u^+ \rangle = \ln(y^+)/0.41 + 5.2$, which is approximately satisfied in the region $30 < y^+ < 180$ at this Reynolds number. The variations in maximum $\langle u^+ \rangle$ can be explained by the differences in computed

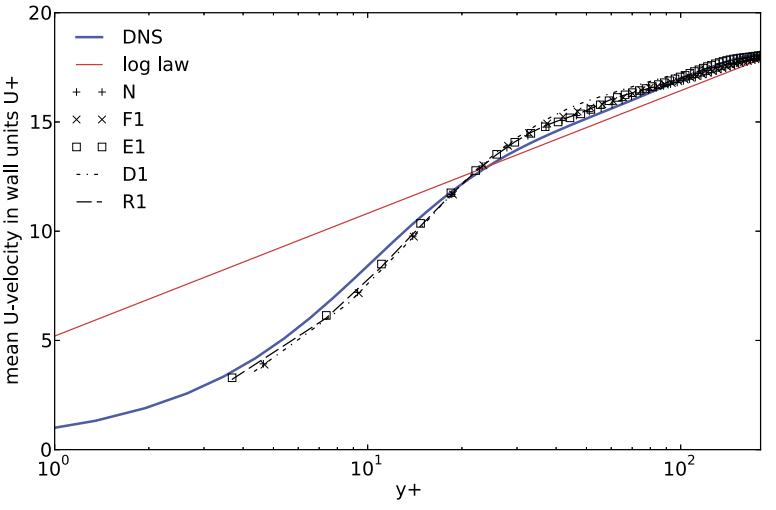

(a) Model comparison

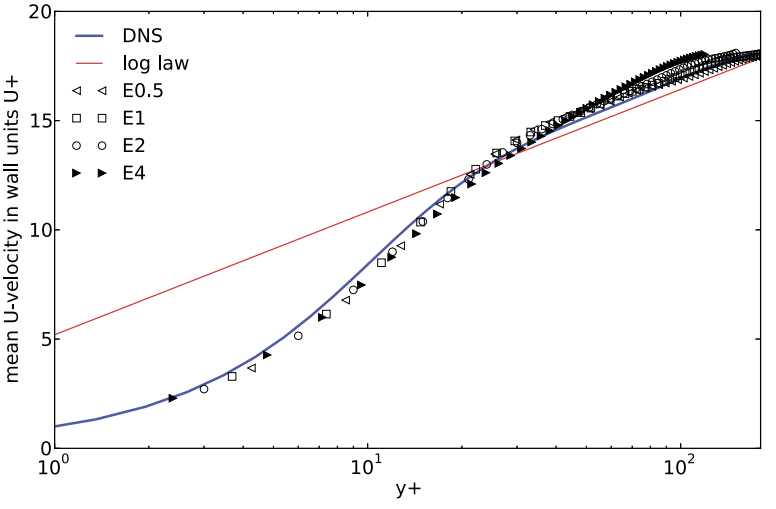

(b) Effect of γ

Fig. 6. Time- and space-averaged velocity in wall units normalised by max. DNS u^+ value, $\langle u^+ \rangle / \max(u^+_{DNS})$.

bulk Reynolds numbers. Even so, the exact SFS and rational LES model results ($\gamma = 1$) almost overlie the DNS data, as expected from the results in Table 3. In Fig. 5 (b), increasing gamma shifts the curves up away from the correct solution.

In Fig. 6, the curves have all been corrected so that the maximum u^+ values are equal to the maximum u^+ value of the DNS data. All the curves in Fig. 6 (a) almost collapse on top of each other, showing good agreement with the DNS data. In Fig. 6 (b), increasing gamma adjusts the shape of the curves away from the correct solution. These effects are shown more clearly in Figs. 7 (a) and (b) where the region $30 \leq y^+ \leq 180$ is magnified. In Fig. 7 (a) the rational LES and exact SFS results ($\gamma = 1$) are on top of each other. This suggests that the fourth-order term in the exact SFS reconstruction makes no real difference to the accuracy, at least in the context of a second-order accurate numerical method. Fig. 8 plots the uncorrected mean velocity on the three meshes using the exact SFS model with $\gamma = 1$, showing convergence towards the true solution.

4.4. Reynolds stresses

Upon time-averaging the filtered Navier–Stokes equations, the Reynolds stresses are given by the sum of the mean velocity fluctuations and the mean SFS stresses. We denote the time-averaged Reynolds stresses by $\langle R_{ij} \rangle = \langle u'_i u'_j + \tau_{SFS,ij} \rangle$. In the results presented, space averaging is performed in addition to time averaging. Fig. 9 shows the normalised Reynolds stress components $\langle R_{11} \rangle / u_\tau^2$, $\langle R_{22} \rangle / u_\tau^2$, $\langle R_{33} \rangle / u_\tau^2$ and $\langle -R_{12} \rangle / u_\tau^2$ (where u_τ is the friction velocity) for the different models with $\gamma = 1$.

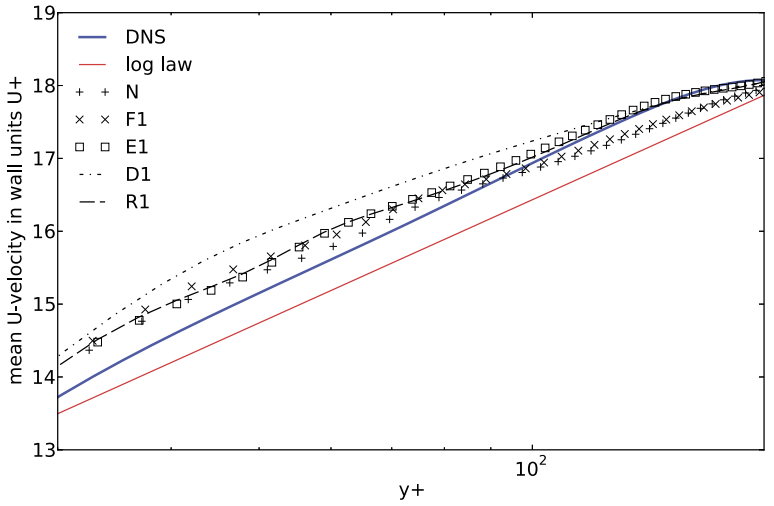

(a)

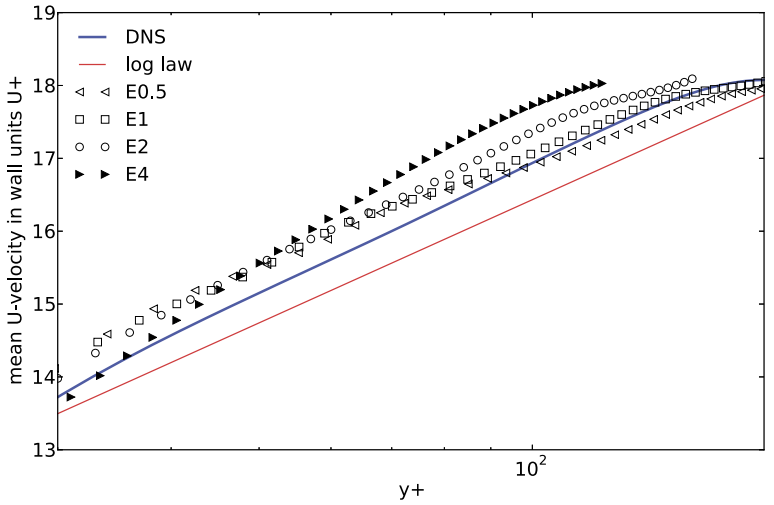

(b)

Fig. 7. Close-up of $\langle u^+ \rangle / \max(u^+_{DNS})$ in range $30 < y^+ < 180$. Legends are the same as Figs. 5, 6.

All simulations over-predict the peak streamwise component $\langle R_{11} \rangle / u_\tau^2$ and deviatoric component $\langle -R_{12} \rangle$. The spanwise and wall-normal components, $\langle R_{22} \rangle$ and $\langle R_{33} \rangle$, are fairly well-predicted, with the exact SFS and RLES models out-performing the others. In turbulent flows, momentum is transferred from fluctuations in the streamwise direction to transverse orientations, and it appears that the RLES and exact SFS models account for this mechanism to a greater degree than the other models. The dynamic Smagorinsky model appears to be no more effective than the absence of a model in this respect. Notably, the near-wall gradients of $\langle R_{22} \rangle$, $\langle R_{33} \rangle$ and $\langle -R_{12} \rangle$ are under-predicted by the dynamic Smagorinsky model, but are quite well captured by the exact SFS and RLES models.

In Fig. 10, γ is varied in the exact SFS model. As γ is increased, the near-wall gradients become steeper. The streamwise component R_{11} is fairly constant with varying γ, but the other components display a marked sensitivity. Overall, $\gamma = 1$ and $\gamma = 2$ are closest to the reference data; $\gamma = 0.5$ under-predicts R_{22} and R_{33} while $\gamma = 4$ has the opposite behaviour. Fig. 11 plots the diagonal components of $\langle R_{ij} \rangle / u_\tau^2$ on the three meshes using the exact SFS model with $\gamma = 1$, showing convergence towards the true solution. Coarser resolutions tend to result in over-prediction of the Reynolds stresses.

4.5. SFS stresses

Fig. 12 shows the space-averaged normalised SFS stress components $\langle \tau_{SFS,11} \rangle / u_\tau^2$, $\langle \tau_{SFS,22} \rangle / u_\tau^2$, $\langle \tau_{SFS,33} \rangle / u_\tau^2$ and $\langle \tau_{SFS,12} \rangle / u_\tau^2$ at the final timestep of each simulation. No time averaging has been applied, which explains the slight lack of smoothness. Since the incompressible Navier–Stokes equations are being solved, the velocity divergence is approximately

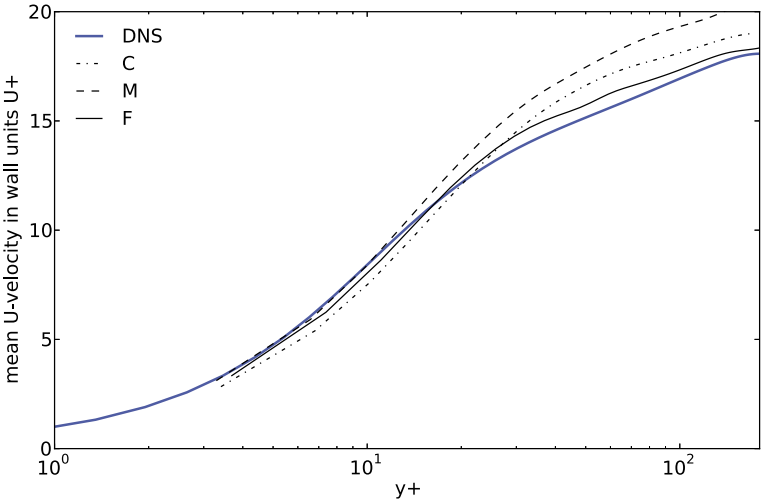

Fig. 8. Time- and space-averaged velocity in wall units $\langle u^+ \rangle$. C = crs, M = med, F = fine mesh. All results using exact SFS ($\gamma = 1$).

zero[1] and therefore diagonal components of the SFS stress calculated by the dynamic Smagorinsky model are zero, while the deviatoric component $\tau_{SFS,12}$ is nonzero. As a consequence, the Poisson equation is solved for a modified pressure $\widetilde{p}'$ incorporating the trace of the SFS stresses. In contrast, the exact SFS and rational LES stresses do not have zero diagonals and the solution of the Poisson equation is the true filtered pressure $\bar{p}$. This may be of some benefit in applications where the pressure must be quantified.

Very little difference is observed between the RLES and exact SFS reconstructions, again implying that the fourth-order term in the exact SFS reconstruction is not significant. Both the exact SFS and rational LES models predict a strong peak in $\langle \tau_{SFS,11} \rangle$ close to the wall. With $\gamma = 1$, the peak value is around 1.75 or $\approx 15\%$ of the peak value of the Reynolds stress $\langle u'u' \rangle$. (When γ is increased, the peak stresses increase considerably.) The peak SFS stress is located at about $y^+ = 10$, within the buffer layer. The peak streamwise velocity fluctuation $\langle u' \rangle$ is at about $y^+ = 20$: i.e., the SFS models provide a mechanism of momentum transfer in a region where the resolved stresses do not. The other SFS stress components reach a peak around $y^+ = 50$–70.

4.6. Flow visualisation

Fig. 13 shows contours of the instantaneous normalised SFS kinetic energy, $k_{SFS} = \frac{1}{2}\tau_{SFS,ii}/u_\tau^2$, in the lower half-channel at time $t = 1000$ using the exact SFS reconstruction. The energy is non-negative everywhere, i.e. local backscattering is not predicted by the model. The energy is concentrated very close to the wall in flattened elongated streaks. Fig. 14 displays contours of the instantaneous Q criterion in the lower half-channel from the exact SFS results, showing the presence of complex vortical structures. Figs. 15 and 16 display the instantaneous streamwise and spanwise vorticity components on horizontal and vertical cut planes respectively, in which coherent flow structures are also visible.

5. Discussion and conclusions

This paper investigates explicit filtering and SFS stress reconstruction using an invertible differential filter for large eddy simulation. The invertibility property allows for exact reconstruction of the resolved SFS stresses. Although this idea has been around for nearly 30 years [8], it has very rarely been tested in actual computations. A number of similar approaches have since been proposed, usually formulated in terms of an approximate inverse filtering operation to simultaneously improve numerical robustness and model the small scales.

The only tunable model parameter in the exact SFS reconstruction is the filter width to mesh size ratio γ. The method can be considered valid in any flow regime, without recourse to arguments based on Kolmogorov's theorems, the Boussinesq hypothesis or any other argument based on fluid physics. That is not to say it guarantees an accurate result from the LES: one must still resolve enough of the turbulent spectrum to capture the important scales in a particular flow. Explicit low-pass filtering and exact SFS reconstruction amounts to re-distribution of energy from poorly-resolved high wavenumbers ($k \geq k_F$) to better-resolved lower wavenumbers ($k < k_F$), improving overall spectral resolution. Unlike adding an SGS closure

[1] Zero divergence is only approximately satisfied when solving the Navier–Stokes equations with a predictor–corrector method, as is the case here. Furthermore, the use of explicit filtering with spatially-varying filter width introduces a commutation error in the continuity equation, preventing the filtered velocity field from being exactly divergence-free.

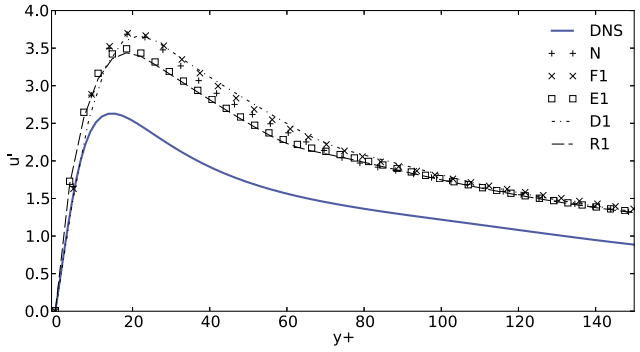

(a) $\langle R_{11} \rangle / u_\tau^2$

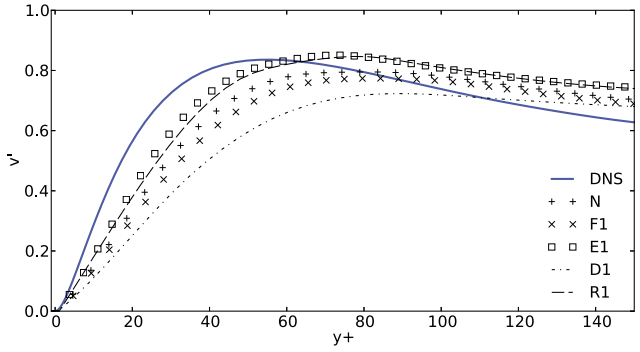

(b) $\langle R_{22} \rangle / u_\tau^2$

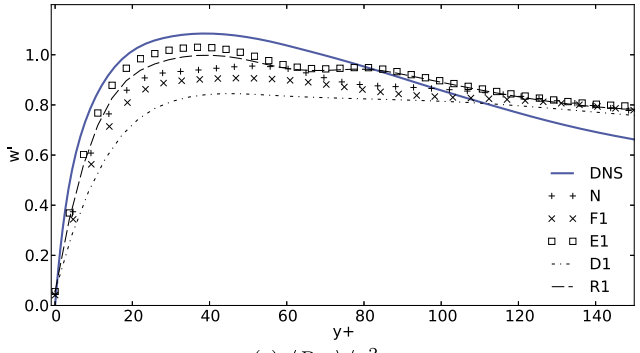

(c) $\langle R_{33} \rangle / u_\tau^2$

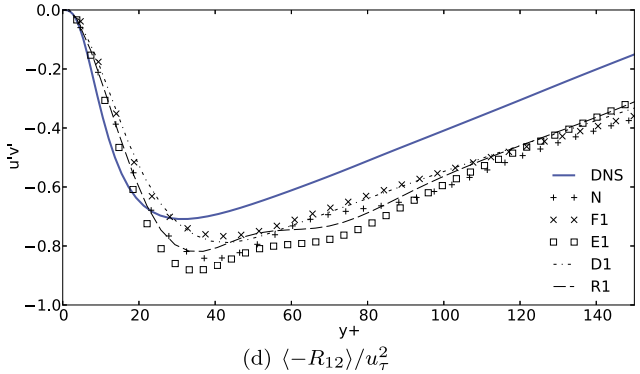

(d) $\langle -R_{12} \rangle / u_\tau^2$

Fig. 9. Normalised time- and space-averaged Reynolds stresses $\langle R_{ij} \rangle / u_\tau^2$. Legend is the same as Fig. 5.

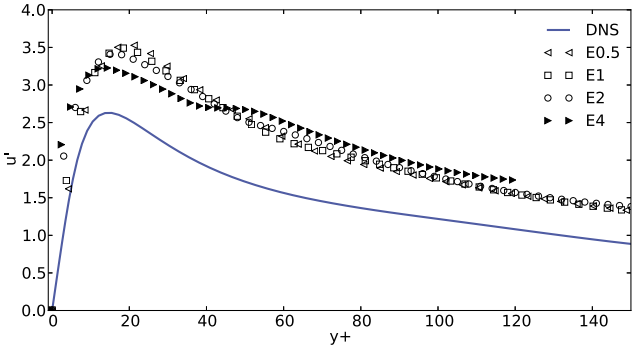

(a) $\langle R_{11} \rangle / u_\tau^2$

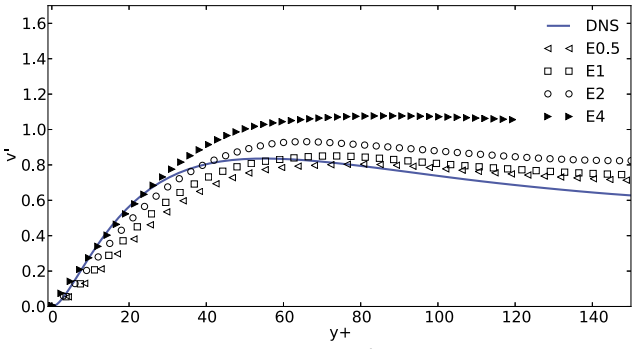

(b) $\langle R_{22} \rangle / u_\tau^2$

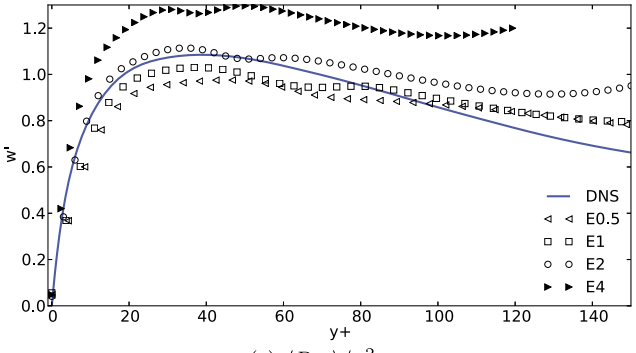

(c) $\langle R_{33} \rangle / u_\tau^2$

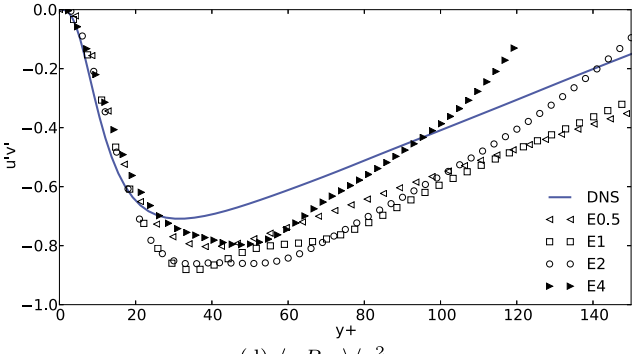

(d) $\langle -R_{12} \rangle / u_\tau^2$

Fig. 10. Normalised time- and space-averaged Reynolds stresses $\langle R_{ij} \rangle / u_\tau^2$. Legend is the same as Fig. 5.

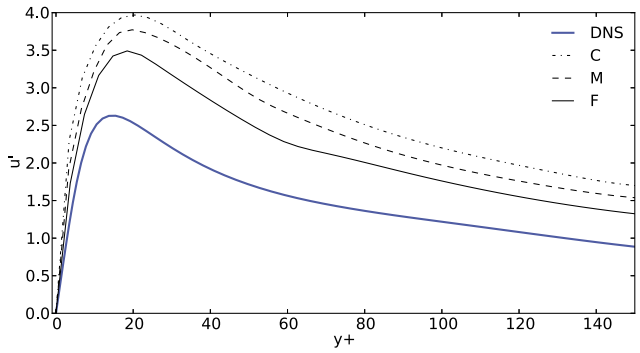

(a) $\langle R_{11} \rangle / u_\tau^2$

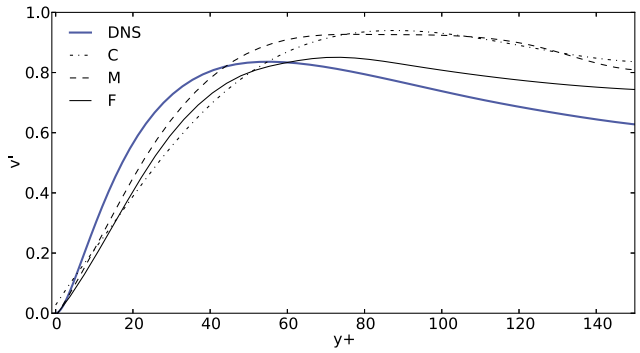

(b) $\langle R_{22} \rangle / u_\tau^2$

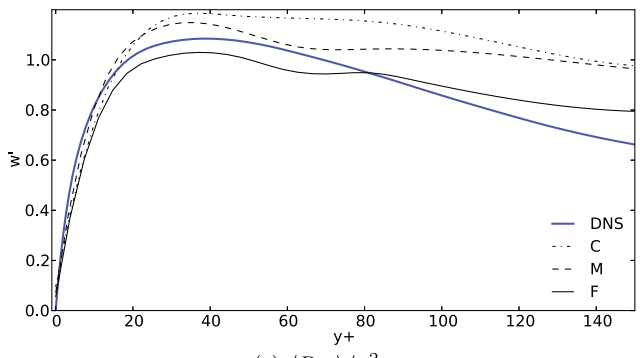

(c) $\langle R_{33} \rangle / u_\tau^2$

Fig. 11. Normalised time- and space-averaged Reynolds stresses $\langle R_{ij} \rangle / u_\tau^2$. C = crs, M = med, F = fine mesh. All results using exact SFS ($\gamma = 1$).

model, the current method does not modify the original equations: it is more of a numerical procedure than a turbulence model.

Recovery of the subgrid-scale stresses, which may contain a significant proportion of the turbulent kinetic energy, is still not possible by the method of reconstruction. Instead of the usual approach of adding an eddy-viscosity type model for the SGS stresses, we simply rely on numerical dissipation from a second-order accurate stabilised finite element discretisation. The extent to which numerical dissipation can represent SGS dynamics depends on the resolution, flow and scheme and is not the subject of the current investigation. At higher Reynolds numbers, it may become necessary to resort to a model for the SGS stresses.

Regarding computational cost, filtering and exact reconstruction requires the solution of six scalar elliptic equations for the six independent components of τ_{SFS}, plus three for the filtered velocity components. While this is not cheap, it is comparable to AD methods which rely on repeated filtering. Furthermore, it has the distinct advantage over AD methods of being applicable to unstructured meshes. The cost could be reduced by considering alternative discretisations. For example, using structured finite differences allows the 3D filtering equation to be reduced to a series of 1D equations involving only the inversion of a tridiagonal matrix. Using spectral methods, the filtering equation is reduced to an algebraic operation in Fourier space [53]. Neither of these options is feasible on unstructured meshes so other methods of reducing the cost should be investigated.

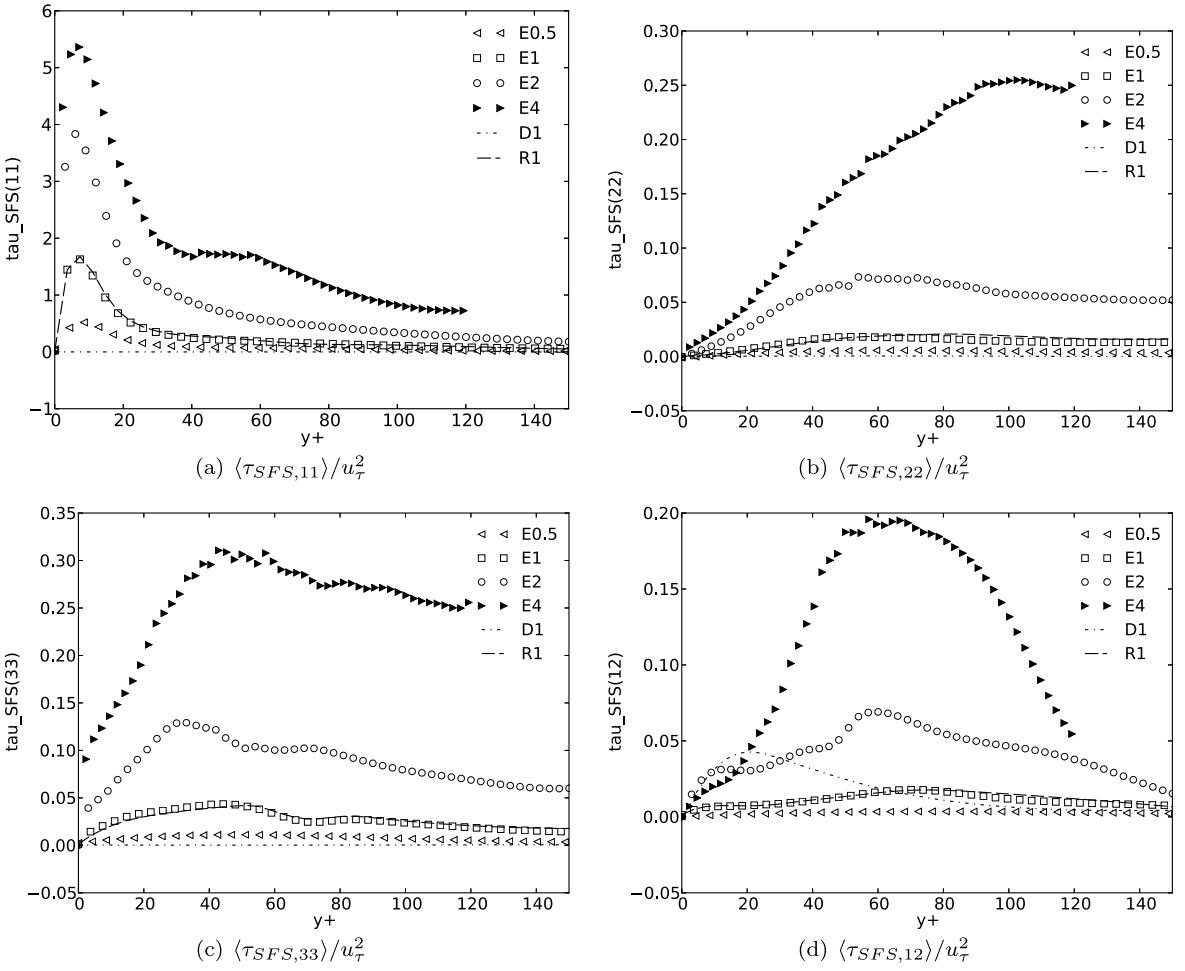

Fig. 12. Space-averaged subfilter stress components. Legend abbreviations are the same as Fig. 5.

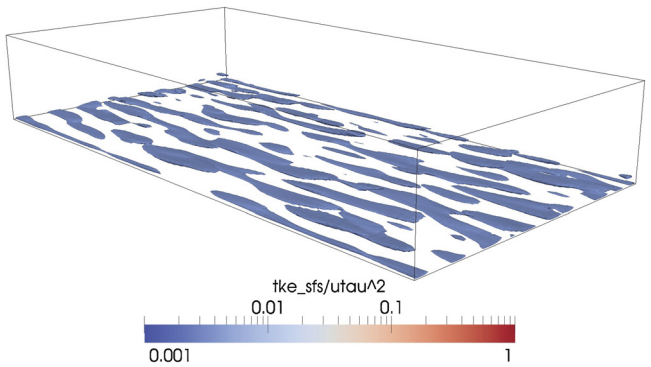

Fig. 13. Contours of subfilter-scale kinetic energy $\frac{1}{2}\tau_{SFS,ii}/u_\tau^2$ in exact SFS computation.

It was discovered that explicitly filtered LES with exact SFS reconstruction predicted several quantities of interest much more accurately than filtering alone, or implicitly filtered LES with the dynamic Smagorinsky model or no turbulence model. Increased accuracy with mesh refinement was demonstrated, which is often difficult to achieve with conventional (implicitly filtered) LES due to the entanglement of numerical and modelling errors. The skin friction coefficient C_f on the fine mesh was very close to the DNS values, implying that near-wall velocity gradients were well resolved. In contrast, the dynamic model and no-model values of C_f were on the low side, implying that the velocity gradients at the wall were not strong enough. This allowed the flow to accelerate under the pressure gradient forcing term calibrated for fully developed channel flow at $Re_\tau = 180$, explaining why the computed Re_τ were too high. Instead of a pressure gradient, one can enforce a con-

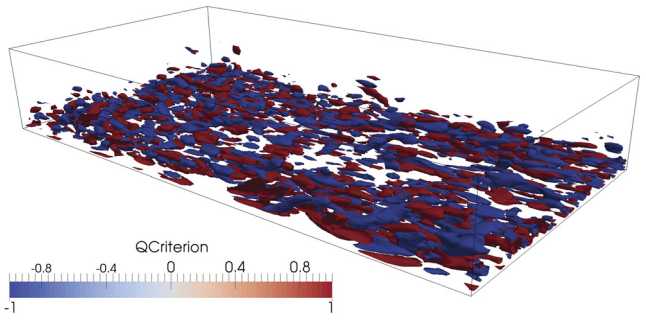

Fig. 14. Contours of Q-criterion in exact SFS computation.

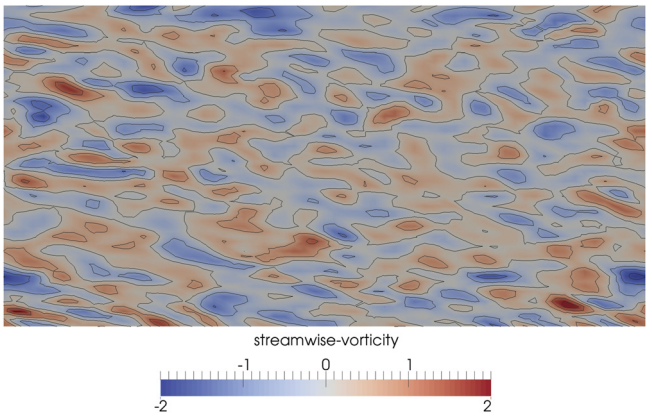

Fig. 15. Streamwise vorticity on horizontal plane at a height 0.002 δ above lower boundary (within first element) in exact SFS computation.

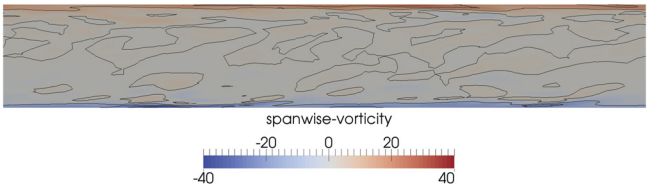

Fig. 16. Spanwise vorticity on vertical mid-plane in exact SFS computation.

stant mass flux through the inlet at every timestep, guaranteeing that the reference conditions are matched. Nevertheless, the mean velocity profiles for all simulations roughly collapsed to the DNS when normalised, showing that slight variations in flow speed did not significantly affect the flow topology and permitting a fair comparison.

Little difference in accuracy was observed between the exact SFS and the rational LES models. The models differ by a term in $\widetilde{\triangle}^4$, and due to the use of second-order numerics this was not expected to have a significant effect. It would be illuminating to conduct the same investigation with a high-order accurate numerical method, and we will pursue this in future work. Numerical dissipation in the second-order method may be excessive in terms of modelling the SGS stresses. A less dissipative second-order method or a higher-order method should be employed instead.

The mesh used in the channel flow had a linear variation of element size $\triangle$ (hence filter width $\widetilde{\triangle}$) in the wall-normal direction. Therefore, the commutation error (26) is of order $\widetilde{\triangle}^2$. Its inclusion into the model could have a beneficial effect on the accuracy of the results, albeit at increased computational expense. In general, the rate of variation of filter width should be controlled such that the error is of at least the order of the numerical scheme. This has consequences for mesh generation, especially in complex domains or if adaptively meshing.

We have shown that explicit filtering with an invertible filter and exact reconstruction of the SFS stresses obtains accurate results in a canonical flow. The potential of this approach for accurate and robust large eddy simulations of challenging flows is considerable. Only the ratio of filter width to mesh size needs to be chosen, and there is good reason to think that this ratio depends solely on the spectral characteristics of the numerical discretisation employed. Future work will be directed at using the method with high-order accurate numerical discretisations and at different invertible filters. Extension of the method to compressible flows has been shown [10] and merits further investigation, in particular in high speed flows with shocks.

Acknowledgements

This research was made possible by the support of the NSF under grant number 1114816, monitored by Dr Leland Jameson, and the Air Force Office of Scientific Research under grant number FA9550-10-1-0418, monitored by Dr Fariba Fahroo.

References

[1] P. Sagaut, Large Eddy Simulation for Incompressible Flows: An Introduction, Springer-Verlag, 2001.
[2] S.B. Pope, Turbulent Flows, Cambridge University Press, 2000.
[3] M. Lesieur, O. Métais, P. Comte, Large-Eddy Simulations of Turbulence, Cambridge University Press, 2005.
[4] A.E. Tejada-Martinez, K.E. Jansen, Spatial test filters for dynamic model large-eddy simulation with finite elements, Commun. Numer. Methods Eng. 19 (2003) 205–213.
[5] J.A. Domaradzki, N.A. Adams, Direct modeling of subgrid scales of turbulence on large eddy simulations, J. Turbul. 3 (24) (2002) 1–19.
[6] S.B. Pope, Large-eddy simulation using projection onto local basis functions, in: J.L. Lumley (Ed.), Lecture Notes in Physics, vol. 566, Springer, 2001, pp. 239–265.
[7] F. Chow, R. Street, M. Xue, J. Ferziger, Explicit filtering and reconstruction turbulence modeling for large-eddy simulation of neutral boundary layer flow, J. Atmos. Sci. 62 (2004) 2058–2077.
[8] M. Germano, Differential filters of elliptic type, Phys. Fluids 29 (6) (1986) 1757–1758.
[9] D. Carati, G.S. Winckelmans, H. Jeanmart, On the modelling of the subgrid-scale and filtered-scale stress tensors in large-eddy simulation, J. Fluid Mech. 441 (2001) 119–138.
[10] A. Jameson, Inverse filtering for compressible flows, unpublished note, http://aero-comlab.stanford.edu/Papers/jameson.fns.pdf, 2003.
[11] S. Stolz, N. Adams, L. Kleiser, An approximate deconvolution model for large-eddy simulation with application to incompressible wall-bounded flows, Phys. Fluids 13 (4) (2001) 997–1016.
[12] J.A. Domaradzki, E.M. Saiki, A subgrid-scale model based on the estimation of unresolved scales of turbulence, Phys. Fluids 9 (7) (1997) 2148–2164.
[13] P. Schlatter, S. Stolz, L. Kleiser, LES of transitional flows using the approximate deconvolution model, Int. J. Heat Fluid Flow 25 (3) (2004) 549–558.
[14] N. Adams, S. Stolz, A subgrid-scale deconvolution approach for shock capturing, J. Comput. Phys. 178 (2002) 391–426.
[15] Y. Zhou, M. Hossain, A critical look at the use of filters in large eddy simulation, Phys. Lett. A 139 (7) (1989) 330–332.
[16] G.S. Winckelmans, A.A. Wray, O.V. Vasilyev, H. Jeanmart, Explicit-filtering large-eddy simulation using the tensor-diffusivity model supplemented by a dynamic Smagorinsky term, Phys. Fluids 13 (5) (2001) 1385–1404.
[17] B.J. Geurts, J. Fröhlich, Numerical effects contaminating LES: a mixed story, in: B.J. Geurts (Ed.), Modern Simulation Strategies for Turbulent Flow, Edwards, 2001.
[18] J. Gullbrand, The effect of numerical errors and turbulence models in large-eddy simulations of channel flow, with and without explicit filtering, J. Fluid Mech. 495 (2003) 323–341.
[19] F. Chow, P. Moin, A further study of numerical errors in large-eddy simulations, J. Comput. Phys. 184 (2003) 366–380.
[20] T.S. Lund, The use of explicit filters in large eddy simulation, Comput. Math. Appl. 46 (2003) 603–616.
[21] S. Bose, P. Moin, D. You, Grid-independent large-eddy simulation using explicit filtering, Phys. Fluids 22 (10) (2010).
[22] P. Fischer, J. Mullen, Filter-based stabilization of spectral element methods, C. R. Acad. Sci., Ser. 1 Math. 332 (3) (2001) 265–270.
[23] B.J. Geurts, D.D. Holm, Alpha-modelling strategy for LES of turbulent mixing, in: Turbulent Flow Computation, 2002, pp. 237–278.
[24] A. Dunca, V. John, Finite element error analysis of space averaged flow fields defined by a differential filter, Math. Models Methods Appl. Sci. 14 (4) (2004) 603–618.
[25] J. Bull, M. Piggott, C. Pain, A finite element LES methodology for anisotropic inhomogeneous meshes, in: K. Hanjalić, Y. Nagano, D. Borello, S. Jakirlić (Eds.), Turbulence, Heat and Mass Transfer, vol. 7, 2012, pp. 317–320.
[26] O.V. Vasilyev, A.L. Marsden, P. Moin, Construction of commutative filters for LES on unstructured meshes, J. Comput. Phys. 175 (2002) 584–603.
[27] A. Petry, A. Awruch, Large eddy simulation of three-dimensional turbulent flows by the finite element method, J. Braz. Soc. Mech. Sci. Eng. 28 (2) (2006) 224–232.
[28] J.A. Domaradzki, Large eddy simulations without explicit eddy viscosity models, Int. J. Comput. Fluid Dyn. 24 (10) (2010) 435–447.
[29] N.J. Georgiadis, D.P. Rizzetta, C. Fureby, Large-eddy simulation: current capabilities, recommended practices, and future research, AIAA J. 48 (8) (2010) 1772–1784.
[30] S. Bose, Explicitly filtered large eddy simulation: with application to grid adaptation and wall modelling, Ph.D. thesis, Stanford University, 2012.
[31] W.J. Layton, R. Lewandowski, On a well pose turbulence model, Discrete Contin. Dyn. Syst., Ser. B 6 (2006) 111–128.
[32] J. Gullbrand, Grid-independent large-eddy simulation in turbulent channel flow using three-dimensional explicit filtering, in: Annual Research Briefs 2003, Center for Turbulence Research, 2003, pp. 331–342.
[33] S. Bose, P. Moin, F. Ham, Explicitly filtered large eddy simulation on unstructured grids, in: Annual Research Briefs, Center for Turbulence Research, 2011, pp. 87–96.
[34] B.J. Geurts, A. Leonard, Is LES ready for complex flows?, in: Closure Strategies for Turbulent and Transitional Flows, 2002, pp. 720–739.
[35] J. Deardorff, A numerical study of three-dimensional turbulent channel flow at large Reynolds numbers, J. Fluid Mech. 41 (2) (1970) 453–480.
[36] M. Germano, Differential filters for the large eddy numerical simulation of turbulent flows, Phys. Fluids 29 (6) (1986) 1755–1756.
[37] R. Clark, J. Ferziger, W. Reynolds, Evaluation of subgrid-scale models using an accurately simulated turbulent flow, J. Fluid Mech. 91 (1) (1979) 1–16.
[38] G. Galdi, W.J. Layton, Approximation of the larger eddies in fluid motions II: a model for space-filtered flow, Math. Models Methods Appl. Sci. 10 (3) (2000) 343–350.
[39] T. Iliescu, P. Fischer, Large eddy simulation of turbulent channel flows by the rational large eddy simulation model, Phys. Fluids 15 (10) (2003) 3036–3047.
[40] J. Serrin, Mathematical principles of classical fluid mechanics, in: Handbook of Physics, vol. VIII/1, Springer, 1959, pp. 125–263.
[41] W. Layton, Weak imposition of "no-slip" conditions in finite element methods, Comput. Math. Appl. 38 (5–6) (1999) 129–142.
[42] S. Bose, P. Moin, A dynamic slip boundary condition for wall-modeled large-eddy simulation, Phys. Fluids 26 (1) (2014).
[43] M. Piggott, G. Gorman, C. Pain, P. Allison, A. Candy, B. Martin, M. Wells, A new computational framework for multi-scale ocean modelling based on adapting unstructured meshes, Int. J. Numer. Methods Fluids 56 (2008) 1003–1015.
[44] D. Davies, C. Wilson, S. Kramer, Fluidity: a fully unstructured anisotropic adaptive mesh computational modeling framework for geodynamics, Geochem. Geophys. Geosyst. 12 (6) (2011).
[45] J. Donea, A. Huerta, Finite Element Methods for Flow Problems, John Wiley & Sons, 2003.
[46] P. Rollet-Miet, D. Laurence, J. Ferziger, LES and RANS of turbulent flow in tube bundles, Int. J. Heat Fluid Flow 20 (1999) 241–254.
[47] F. Sotiropoulos, S. Abdallah, The discrete continuity equation in primitive variable solutions of incompressible flow, J. Comput. Phys. 95 (1991) 212–227.

[48] C. Pain, M. Piggott, A. Goddard, F. Fang, G. Gorman, D. Marshall, M. Eaton, P. Power, C. Oliveira, Three-dimensional unstructured mesh ocean modelling, Ocean Model. 10 (2005) 5–33.
[49] J. Kim, P. Moin, R. Moser, Turbulence statistics in fully developed channel flow at low Reynolds number, J. Fluid Mech. 177 (1987) 133–166.
[50] C. Geuzaine, J.-F. Remacle, Gmsh reference manual, Montefiore Institute, University of Liège Dept. of Electrical Engineering and Computer Science, Liège, Belgium, 2009, http://www.geuz.org/gmsh/.
[51] S. Balay, J. Brown, K. Buschelman, V. Eijkhout, W.D. Gropp, D. Kaushik, M.G. Knepley, L.C. McInnes, B.F. Smith, H. Zhang, PETSc users manual, Tech. Rep. ANL-95/11, Argonne National Laboratory, USA, 2010, revision 3.1.
[52] P. Andersson, L. Brandt, A. Bottaro, D. Henningson, On the breakdown of boundary layer streaks, J. Fluid Mech. 428 (2001) 29–60.
[53] P. Moin, Fundamentals of Engineering Numerical Analysis, Cambridge University Press, 2001.